Effect of Stopper-Rod Misalignment on Fluid Flow in Continuous Casting of Steel

R. CHAUDHARY, GO-GI LEE, B.G. THOMAS, SEONG-MOOK CHO, SEON-HYO KIM, and OH-DUCK KWON

Misalignment of metal-delivery systems can cause asymmetric fluid flow in the mold region of continuous casters, leading to abnormal surface turbulence, insufficient superheat transport to the meniscus, slag entrainment, inclusion entrapment, and other quality problems. This work investigates the effect of stopper-rod misalignment on nozzle and mold flow velocities in a conventional continuous casting process using both a water model and a computational model. Three stopper-rod configurations are studied (aligned, front misaligned by 2 mm, and left misaligned by 2 mm). The 3-D steady k–ε finite-volume model matched well with impeller probe measurements of both velocity and its fluctuations. Negligible asymmetry was found near the narrow faces. Asymmetry close to submerged entry nozzle is the main cause of vortex formation observed in all cases. The left-misaligned stopper-rod produces a shallower jet with a higher flow rate from the right port, leading to higher surface velocities on the right surface. This produced substantially more large vortices on the left side. The asymmetry produced by the nozzle length bore diameter ratio of ~21 in this work is consistent with the theoretical critical entrance length of ~24 for turbulent pipe flow.

DOI: 10.1007/s11663-011-9478-5

I. INTRODUCTION

CONTINUOUS casting solidifies most steel worldwide.[1] Final product quality depends greatly on the flow pattern of molten steel in the mold, especially near the top surface. To avoid surface defects, and internal inclusions from slag entrainment, the surface velocity and turbulence levels need to be maintained within an optimum range.[2,3] Turbulent flow in the mold of a continuous caster is governed by the geometries of the nozzle, mold, and flow control surfaces (slide-gate or stopper-rod), casting speed, argon gas injection, and electromagnetic forces.[2]

Asymmetric flow causes transient fluctuations and is a main cause of product defects.[4–6] Asymmetric flow causes high surface velocity on one side and causes low surface velocity on the other. This causes transient cross-flow between the narrow gap between the submerged entry nozzle (SEN) and the mold, leading to surface defects, vortex formation, slag entrapment, and other defects.[5,6] In addition to aggravating turbulent fluctuations and the associated intermittent problems, asymmetric flow can create a constant flow bias on the top surface of the mold, which increases the chance for velocity on one side to exceed the critical range, leading to slag entrainment[4,5] and accompanying sliver defects.[4,5,7] At the same time, it may cause insufficient velocity on the other side, leading to meniscus freezing and associated surface defects.[2]

Previous researchers have studied the effects on nozzle and mold flows of various asymmetries, including turbulence,[8] slide-gates,[9–11] nozzle clogging,[12] and misaligned nozzles.[13–17] Yuan *et al.*[8] performed large eddy simulation (LES) to study the natural transients and asymmetries associated with turbulent flow in otherwise symmetric "quasisteady" flow conditions. Flow in the mold cavity switched between double-roll and complex flow patterns with many vortices. Bai *et al.*[9,10] studied the effect of slide gate orientation on asymmetric flow. A 90-deg (front–back) gate orientation caused swirl in the jet leaving the nozzle, whereas a 0-deg (right–left) orientation caused severe right–left flow asymmetry, with more than 2/3 of the mass flow leaving the right port for a 50 pct open gate. Lee *et al.*[11] found that front–back asymmetry caused by a 90-deg slide-gate was responsible for particle entrapment on the inner radius. Mahmood[12] computed the asymmetric flow caused by nozzle clogging based on clog samples collected at the steel plant. A two-fold difference in surface velocity between opposite sides of the SEN leading to vortex formation was found. Asymmetric effects were enhanced by increasing casting speed and reducing SEN depth.[5,6,12] Modeling by Zhang *et al.*[13] found a similar great effect of SEN clogging on

R. CHAUDHARY, Ph.D. Student, and B.G. THOMAS, Professor, are with the Department of Mechanical Science and Engineering, University of Illinois at Urbana-Champaign, Urbana, IL 61801. Contact e-mail: bgthomas@illinois.edu GO-GI LEE, Senior Researcher, is with the Non-Ferrous Refining Project Team, Research Institute of Industrial Science and Technology, Pohang, Kyungbuk 790-784, South Korea. SEONG-MOOK CHO, Ph.D. Student, and SEON-HYO KIM, Professor, are with the Department of Materials Science and Engineering, Pohang University of Science and Technology, Pohang, Kyungbuk 790-784, South Korea. OH-DUCK KWON, Quality & Technical Team Leader, is with the Magnesium Business Department, POSCO, Suncheon, Jeonnam 540-856, South Korea.
Manuscript submitted February 20, 2010.

Published online: 08 February 2011

asymmetric flow, causing increased slag entrainment, inclusion entrapment, and possible breakouts because of excessive local superheat impingement. Yokoya *et al.*[14] used water model experiments and computational predictions to study the effect of off-centered SEN in billet casting. Similar to slab casting, surface flow was predicted through the gap between the nozzle and the mold because of this asymmetry. Water model studies by Gupta *et al.*[15] found that off-centering the nozzle along the wide faces by more than 4 pct of the mold width caused noticeable asymmetries in the time-averaged flow in the mold. The flow asymmetry was observed to persist deep into the liquid pool many meters below the meniscus.[16] Li *et al.*[17,18] concluded that the size and intensity of vortexing depends on the off-centeredness of the SEN and the casting speed.

Another potential cause of detrimental asymmetric flow is stopper-rod misalignment. Stopper misalignment may be caused by accidental faulty placement, buoyancy forces caused by the density difference between the light-weight ceramic stopper-rod and the molten steel, thermal distortion of the support beams caused by radiation heat from the steel pool below, and drag force caused by cross flow in the tundish. These effects on mold flow and vortex formation are unknown. Flow with stopper-rod control generally is considered to be much more symmetrical than with slide gates. Considering the variations of turbulent fluctuations, however, it is not easy to indentify whether an extra asymmetry is caused by the stopper or not. Yuan *et al.*[19] and Mahmood[12] reported significant asymmetric flow just below the stopper, especially if cross-flow occurs across the bottom of the tundish, but the consequence to mold flow was not studied. The current work focuses on quantifying the effect both numerically and experimentally of stopper-rod misalignment on nozzle flow, mold flow, and vortex formation in a one-third scale water model of a continuous casting process.

II. INVESTIGATION METHODS

A. *Water Model Experiments*

The effect of stopper-rod misalignment was investigated experimentally using a one-third–scale water model of the steel caster at Gwangyang Works, POSCO, South Korea. Figure 1 shows a schematic of the one-third–scale water model. During operations, water is pumped from a water storage bath below the mold tank into the tundish through a flow meter. From the tundish, water falls via gravity through the stopper head region, SEN bore, and exit ports into the mold cavity. Water exits the bottom of the mold through 11 outlets of 25-mm diameter and passes through a flow meter before entering the water bath again. The two flow meters (before tundish and after mold) along with the stopper-rod and variable-speed pump control the flow rate in the mold to maintain the desired surface level.

To perform water model measurements, the stopper-rod either was aligned or moved 2 mm toward the front or toward the left to investigate misalignment, as shown in the top view in Figure 2. Impeller velocity probes were positioned 15 mm below the top free surface on both sides of the SEN at either 150 or 60 mm from narrow faces (NFs) to measure horizontal surface velocities as shown in Figure 3(a). Instantaneous surface velocity data were collected at a sampling frequency of 1 Hz. Each probe is a 35-mm-long, open-ended tube (22-mm inner and 28-mm outer diameter) containing a small propeller that rotates in proportion with the water flow speed as shown in the close-up in Figure 3(b). The probe has a total response time of ~10 seconds (*i.e.*, 0.1 Hz), including electrical response time (~0.4 seconds to reach 63 pct of end value) and mechanical response time (for the vanes to respond to increase or decrease in flow). The probes are accurate over the velocity range of 0.02 to ~5 m/s. For each case, mean velocities were averaged up to 2000 seconds, and corresponding isotropic turbulent kinetic energies were derived using the standard root mean square relation,[20] assuming unmeasured components had the same variations. Table I gives operational details on the water model measurements and additional data are given elsewhere.[21]

To visualize vortex formation, sesame seeds were added to the top surface as tracer particles and vortexing phenomena were recorded with a high-speed video camera. The number and location of all vortices lasting at least 2 seconds were measured from the high-speed video. The total number of vortices observed at each location then was divided by the total recording time (10 minutes) to calculate vortex formation frequency.

B. *Computational Model*

To augment the experimental investigation, a three-dimensional (3-D) finite-volume computational model has been formulated to investigate the time-averaged turbulent flow in the nozzle and the mold with aligned and two misaligned (front and left) positions of the stopper-rod as shown in the top view in Figure 2. The steady-state, incompressible, Navier–Stokes equations with a standard k- and ε-turbulence model (Launder and Spalding[22]) have been solved in FLUENT[23] to simulate the time-averaged turbulent flow.

To minimize computational effort, symmetry was exploited. One-quarter nozzle and mold domains were used to simulate flow with the aligned stopper-rod. Figure 4(a) shows the quarter nozzle with mesh with the aligned stopper-rod case. For front and left misalignments, right- and back-half domains were used, respectively. A similar mesh to the aligned case was used for the misaligned cases with 54,000 hexahedral cells in the back half for left misalignment and 33,000 hexahedral cells in the right half for front misalignment. Figure 4(b) shows the stopper head region of the upper tundish nozzle (UTN) and dimensions for these misaligned cases. To model the flow entering the stopper-head region, a cylindrical portion of the tundish bottom (with 200-mm diameter and 150-mm height) is created above the SEN. Figure 5 shows the typical back-half mold domain with mesh used in the left misalignment of the stopper-rod.

To improve efficiency and convergence, nozzle flow is simulated first, assuming a pressure outlet boundary

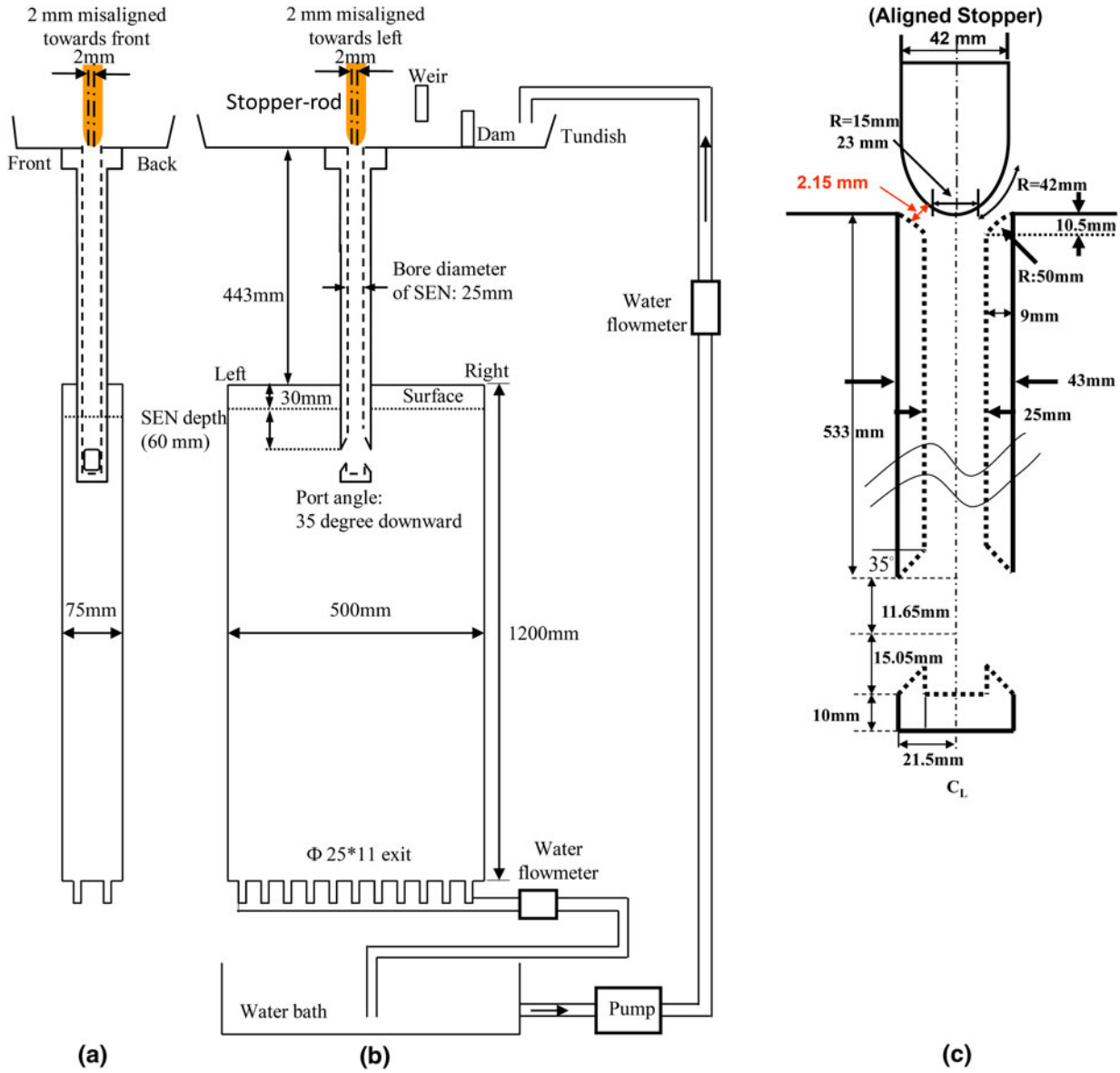

Fig. 1—Schematic of the one-third water model showing 2-mm stopper-rod misalignment (*a*) right-side view, (*b*) front view, and (*c*) close look at aligned stopper-rod nozzle.

condition at the port exit planes. The velocities, turbulent kinetic energy, and dissipation rate at the outlet from the nozzle ports then are applied as boundary conditions for the inlet to the mold. Hershey *et al.*[24] showed that this approach matches well with the results of simulations that combine the nozzle and the strand together. Convergence is easier because residuals in the important low-velocity regions of the strand are not overly influenced by small errors in the high velocities inside the nozzle. The meshes of the nozzle outlet and the strand inlet were identical with one-to-one mapping to ensure accurate flux balance between the two computational domains.

Average velocity, kinetic energy k, (10^{-5} m^2/s^2), and its dissipation rate ε, (10^{-5} m^2/s^3) were fixed at the circumference and the top annular region of the cylinder (representing part of the tundish) to match the flow rate required for the casting speed of 0.917 m/min. The top free surface was assumed flat with a free-slip boundary condition. The free surface level profile was calculated from the pressure distribution along this free surface based on the potential energy conservation.[25,26] Like the steel caster, the strand outlet was modeled with no bottom and a constant-pressure outlet boundary condition. The water model bottom deflects the flow somewhat, but this difference is expected to be small because of the long domain and is limited to the lower region. To handle reverse flow from the strand exit in the lower recirculation zone, small values of k and ε (10^{-5} m^2/s^2 and 10^{-5} m^2/s^3) were set at the strand domain exit, along with 0-Pa gauge pressure. The vertical wide and NF walls were considered stationary. Standard wall laws were used as boundary conditions for all walls.[27] Table I gives various process parameters, physical properties of water, and dimensional details about the one-third water model.

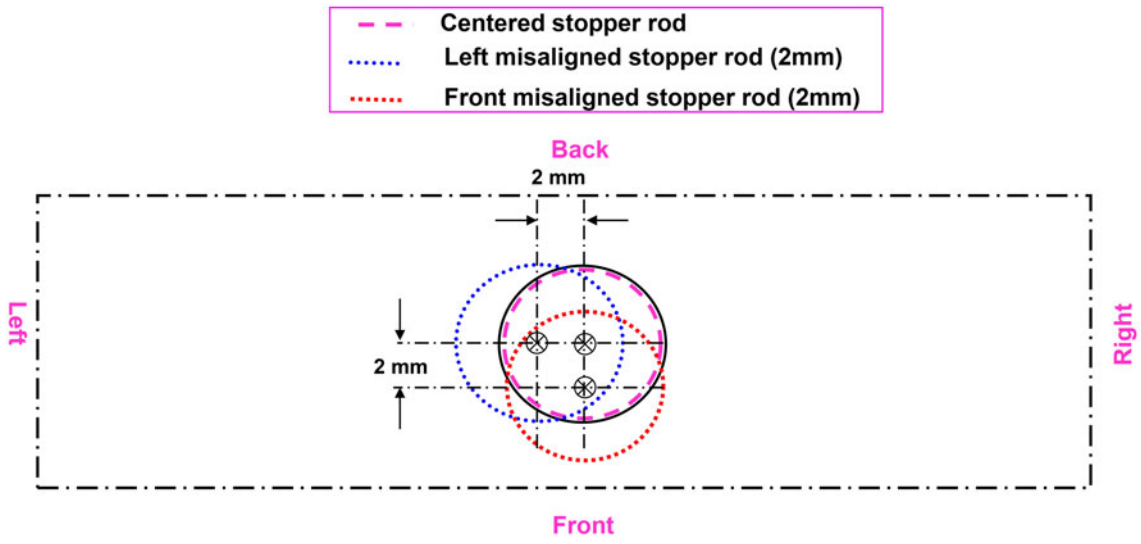

Fig. 2—Top view of three stopper-rod positions studied.

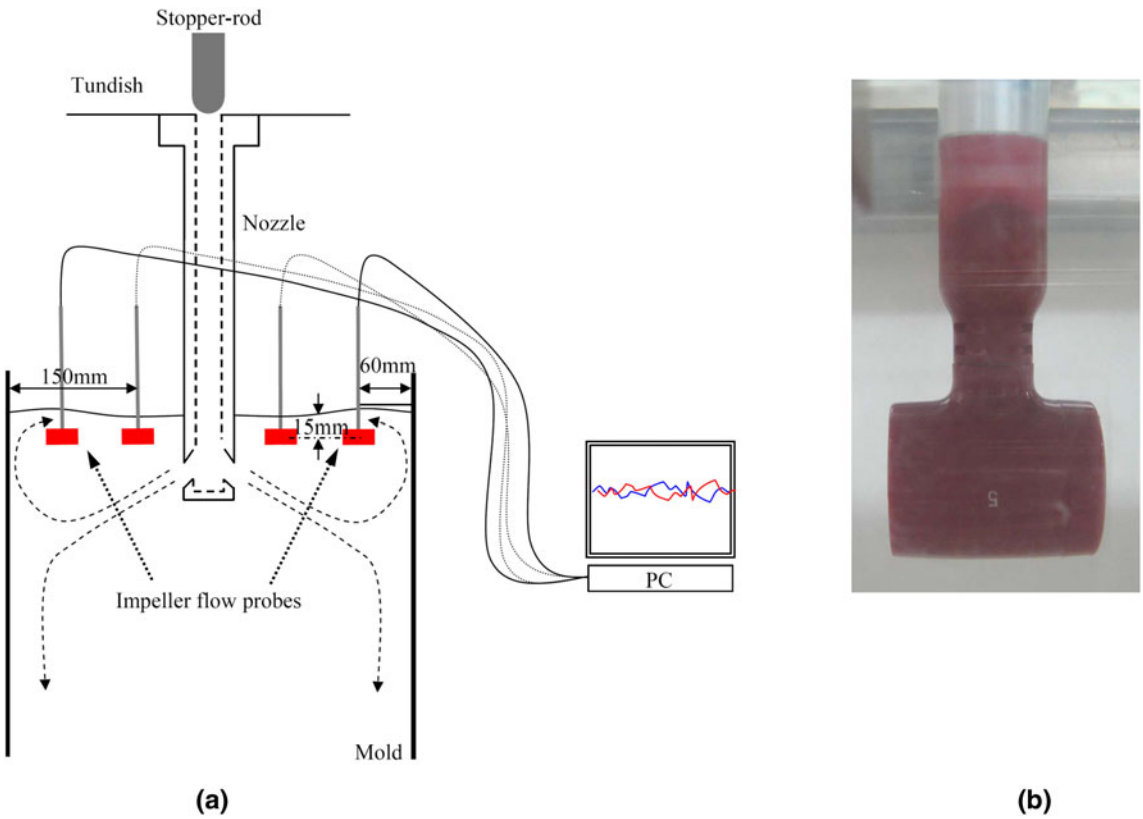

Fig. 3—(*a*) Schematic of the impeller probe with locations and (*b*) close up of the probe.

The equations for the three momentum components, k-, ε-, and pressure Poisson equation are discretized using the finite volume method in FLUENT[20] with first-order upwind scheme for convection terms. These discretized equations then are solved for velocity and pressure using the Semi-Implicit Pressure Linked Equations algorithm, starting with the initial conditions of zero velocity in the whole domain. The segregated solver in FLUENT was used to solve all equations. In all simulations, convergence was defined when all scaled residuals were reduced below 10^{-4}. All computations were performed on a PC with a 2.66 GHz Intel Xeon processor (Intel Corp., Santa Clara, CA) and 4.0 GB RAM. Additional details about the computational model are given elsewhere.[24,28,29]

Table I. Process Parameters for Experimental Setup and Numerical Simulations in One-Third Water Model

Casting speed	0.917 m/min
Water flow rate	34.4 LPM
Mold width	500 mm
Mold thickness	75 mm
Computational domain width	250 mm
Computational domain thickness	37.5 mm
Computational domain length	1200 mm
SEN depth	60 mm
ρ_{fluid}	998.2 kg/m^3 (water)
μ_{fluid}	0.001 kg/m s (water)
Stopper-rod	Centered (*i.e.*, aligned), front, and left misaligned (2 mm)
Nozzle port angle	35 deg
Nozzle port area	23.3 mm (width) × 26.7 mm (height)
Nozzle bore diameter (inner/outer)	25 mm/43 mm
Distance between tundish bottom and nozzle bottom	560 mm
Shell	no
Gas injection	no

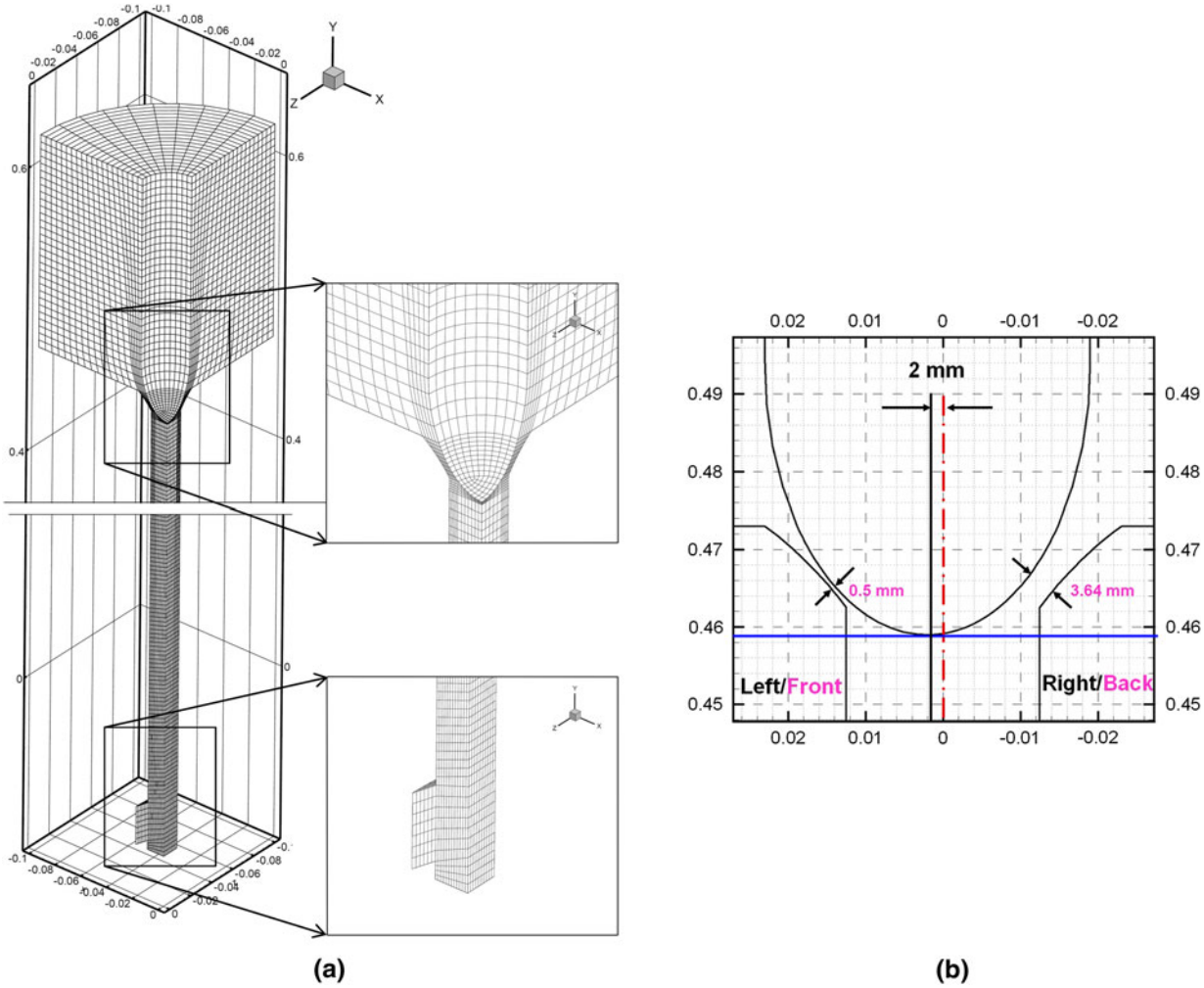

Fig. 4—(*a*) Centered stopper-rod with nozzle (quarter nozzle: 22,400 hexahedral cells) and (*b*) dimensional details after misalignment.

III. MODEL VALIDATION

The computational model first was validated by comparison with the near-surface velocities measured by the velocity probe on both sides of the SEN. Mean velocities ($\bar{u}$), turbulent kinetic energies (k), and standard deviations (σ) were calculated from 1000 or

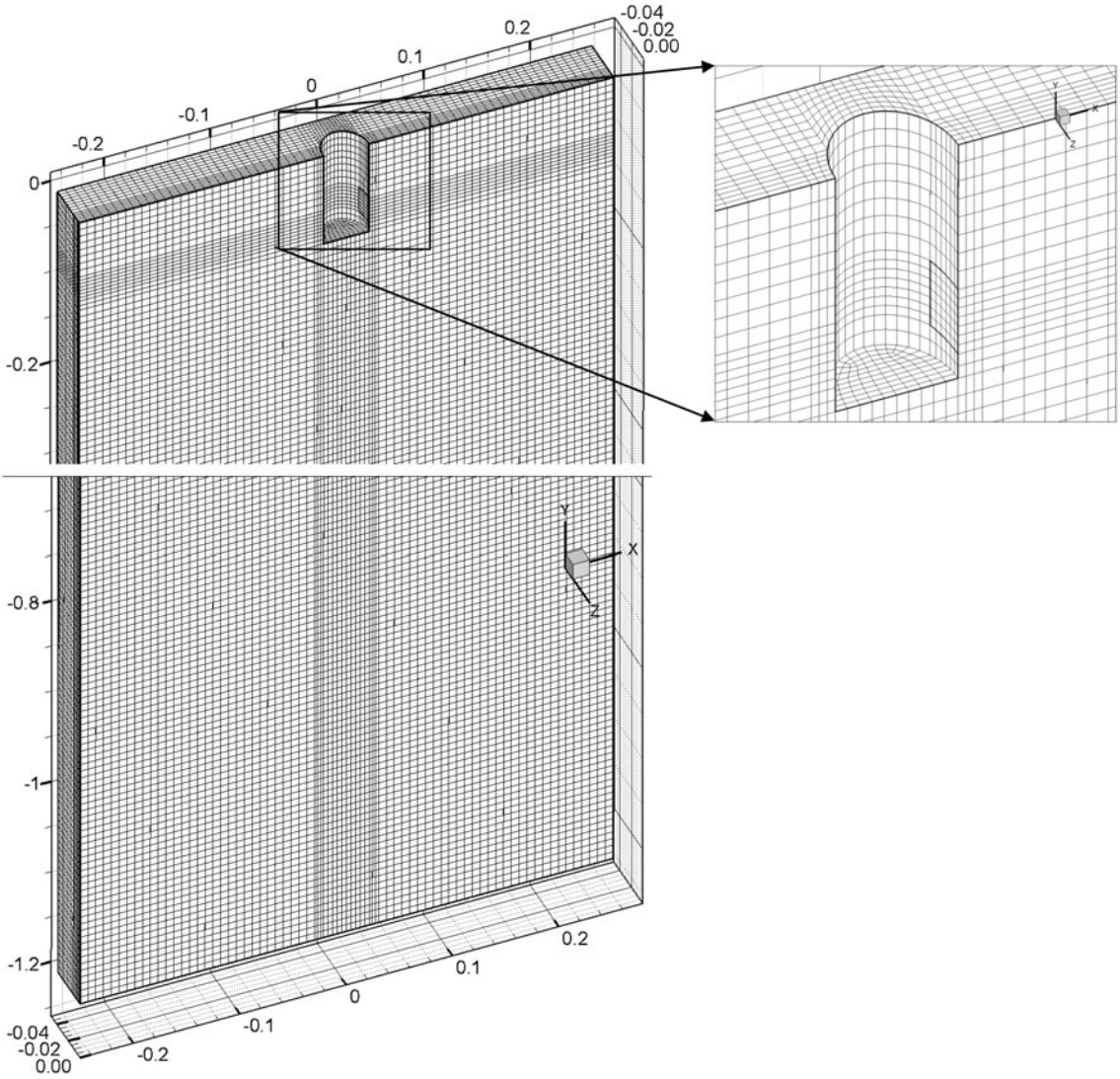

Fig. 5—Back-half mold mesh (90,000 hexa-cells in quarter mold, *i.e.,* 360,000 hexa-cells in full mold).

Table II. Comparison of Mean Near-Surface Velocities Between Computational Predictions and Experiments at Four Locations

	Unit (m/s)	60 mm from Left NF	150 mm from Left NF		150 mm from Right NF	60 mm from Right NF
Aligned	measurements	0.093	0.098	Nozzle	0.103	0.094
	standard deviation	0.018	0.018		0.019	0.022
	model predictions	0.102	0.120		0.120	0.102
Front misaligned	measurements	0.094	0.105		0.096	0.096
	standard deviation	0.018	0.019		0.018	0.021
	model predictions	0.097	0.122		0.122	0.097
Left misaligned	measurements	0.096	0.084		0.111	0.105
	standard deviation	0.023	0.016		0.018	0.017
	model predictions	0.084	0.060		0.104	0.095

2000 seconds of instantaneous measured velocity data in different cases using the following equation:

$$k = (3/2)\sigma^2 = (3/2)(1/N)\sum_{n=1}^{N}(u_i - \bar{u})^2 \qquad [1]$$

where N is the total number of measured data points and u_i is the instantaneous horizontal surface velocity. This equation to estimate the measured k assumes isotropic turbulence.

Table II compares time-averaged surface velocities of the computational model and measurements.

The measured standard deviations were ~0.02 m/s (or ~20 pct of the mean). The mean velocity predictions fall within the range of +/– one standard deviation of the mean of the measurements in all cases. Errors are generally less than 9 pct at 60 mm from the NFs and less than 25 pct at 150 mm. The only exception is for the left misalignment case on the left side in which the maximum error is 13 pct at 60 mm and 40 pct at 150 mm. The larger error at this location is because of the complex vortex flow pattern found at this location not being resolved as accurately by the current Reynolds–Averaged Navier–Stokes (RANS) k–ε turbulence model. The computational model predicts a higher surface velocity at 150 mm from NF relative to 60 mm because this location is closer to halfway between the SEN and the NFs. Surprisingly, the experiments give similar velocities at 150 and 60 mm from the NFs.

The experiments and simulations exhibit the same trends. Measurements for the aligned and front-misaligned cases show the expected right–left symmetry within ~5 pct, which is less than the standard deviation of the measurements of ~20 pct. This symmetry is imposed in the computational model. Left misalignment causes significant right–left asymmetry, with the right side having a higher surface velocity.

Table III compares the computed turbulent kinetic energy with values extracted from the measurements using Eq. [1]. Turbulent kinetic energy matches well (same order) with the measurements in all cases. The largest differences are observed on the left side of left misalignment because of complex vortex formation. The vortices increase the measured turbulence, but are not captured perfectly by the computational model. Overall, the observed differences are reasonable considering the anisotropy of real turbulence, total measurement time, sampling frequency, probe response time, and numerical errors (truncation and round-off).

For consistency, all simulations were performed with the standard k–ε model with standard wall laws. This simple, readily available model has reasonable accuracy in a wide range of flows and excellent computational efficiency. It is not the best for asymmetric flow with vortex formation. However, other RANS models produced similar or worse behavior for the current problem. Time-varying models (such as direct numerical simulation (DNS), LES) may perform better but are computationally intensive. An extensive investigation of the advantages and disadvantages of various flow models is reported elsewhere.[29]

IV. NOZZLE FLOW RESULTS

A. *Effects Near Stopper Head*

The effect of stopper misalignment on flow near the stopper head and tundish bottom is presented in Figure 6. As expected, high velocity flow is predicted through the restricted flow area between the stopper-head and the curved tundish bottom or UTN. Much less flow passes through the most restricted side because of higher pressure loss. In left/front misalignment, only ~15 pct (~0.08 kg/s) of the flow rate is from the restricted left/front quarter of the nozzle near the stopper head with the remaining ~35 pct (~0.20 kg/s) pouring through the larger quarter opening on the right/back side. The symmetric flow through the aligned one-quarter nozzle model is 25 pct (~0.14 kg/s).

Stagnation regions exist under the stopper-head and along the SEN bore wall below the curved tundish bottom. For the misaligned cases, Figure 6(b) shows the increased velocity (18 pct higher than average) through the larger high-flow area, which is the right side in the left misalignment and the back side in front misalignment. This creates higher momentum steel falling from this side toward the opposite side of the SEN bore wall. Velocity is lower on the restricted, low flow rate side. Figure 6(c) shows the cross section perpendicular to the section shown in Figure 6(b) for the front/left misalignment cases. Here, the stagnation region below the stopper-head is lessened because of the high-momentum flow crossing sides in the other plane.

B. *Effects Near SEN Ports*

Velocity magnitude contours and streamlines near the bottom well of the SEN are presented in Figure 7 for the same three alignment cases. The aligned stopper-rod shows a 14 pct shorter jet at the port exit (centerplane) compared to the front misaligned and left side of the left-misalignment cases. The jet on the right side in left misalignment has the maximum height (~28 pct more than on the left side). The higher momentum of flow down the left side of the nozzle bore with left misalignment also is shown in Figure 7(c). Figure 8 and Table IV respectively show the flow patterns and jet characteristics[30] at the ports for the aligned, front-, and left-misaligned stopper-rod cases. The jets from the aligned stopper-rod case are naturally front–back symmetric, with 19 pct reverse-flow area on the top of the port. The vertical jet angle, horizontal spread angle, weighted

Table III. Comparison of Turbulent Kinetic Energy Between Computational Predictions and Experiments at 150 mm and 60 mm from NFs on Both Sides of the SEN

	Unit (mm^2/s^2)	60 mm from Left NF	150 mm from Left NF		150 mm from Right NF	60 mm from Right NF
Aligned	measurements	486	472	Nozzle	530	691
	model predictions	690	375		375	690
Front misaligned	measurements	479	552		507	637
	model predictions	724	533		533	724
Left misaligned	measurements	822	404		488	425
	model predictions	357	140		300	502

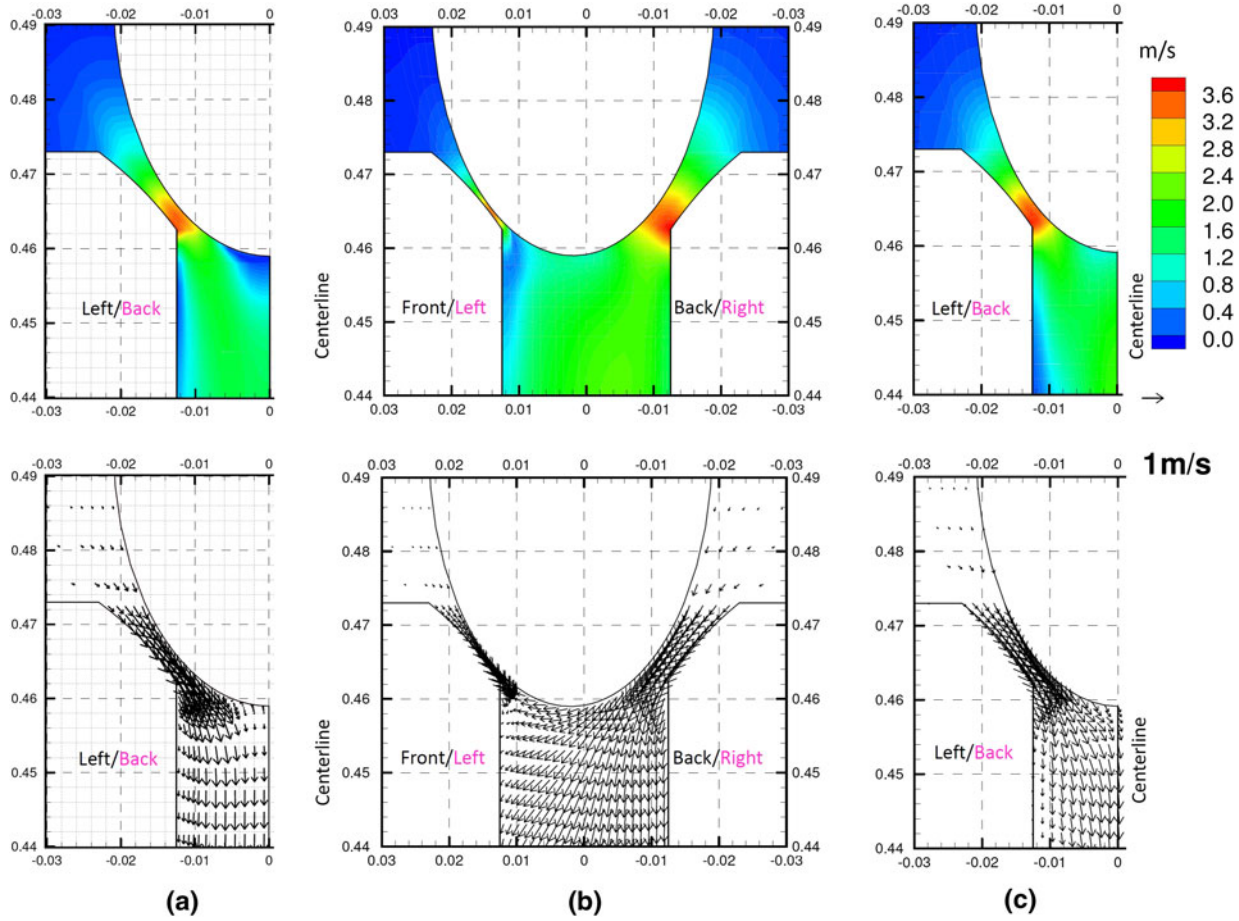

Fig. 6—Velocity contours and vectors near stopper-rod head region at the center plane with (*a*) aligned, (*b*) 2-mm front (side view)/left (front view) misaligned, and (*c*) 2-mm front (front view)/left (side view) misaligned stopper-rod.

turbulent kinetic energy, and dissipation rate in the aligned stopper case are higher than in any of the misaligned cases. In the front-misaligned stopper-rod case, the jet is bent toward the back causing front–back asymmetry but still has the same reverse flow fraction (19 pct) as in the aligned stopper-rod. The left side jet in the left-misaligned case has a higher reverse flow port area (28 pct) than the right side (12 pct) and any other jet. The jet with left misalignment naturally is front–back symmetric but has right–left asymmetry. Although the flow exiting the left-side port with the left-misaligned stopper-rod is smaller than the right, the average jet speed on the left side is higher.

Usually, the effect of inlet velocity asymmetries in turbulent pipe flow should disappear if the following is true[31]:

$$\frac{L}{D} > 4.4\mathrm{Re}^{1/6} \qquad [2]$$

where $\mathrm{Re} = DU\rho/\mu$, L is pipe length, D is pipe diameter, U is mean axial velocity, ρ is density, and μ is molecular viscosity. For the current water model, Eq. [2] predicts a critical L/D of ~24. Because the current water model has a smaller L/D (SEN bore length [from tundish bottom to ports]/bore diameter) of ~21, the effects of stopper misalignment are expected to persist past the SEN ports. This is consistent with the findings of this work. Extending Eq. [2] to the real caster, in which the casting speed of 1.6 m/min is root(3) times faster than speed in the Froude-scaled, one-third-scale water model,[32] the critical (L/D) increases to ~32. Thus, asymmetry effects are expected to be at least as strong in the real steel caster, as those found in this work.

V. MOLD FLOW RESULTS

A. *Flow Pattern*

Mold flow patterns for the aligned, front-, and left-misaligned stopper-rods are presented in Figure 9. Overall, the flow is a classic "double-roll" in all cases, as the jets impinge first upon the NFs then flow up and back across the surface toward the SEN.

With the aligned stopper-rod case, the jet flows mostly toward the NF. With front misalignment, more flow exits the front side of the ports but the jet bends toward the back mold face (outer radius) as is shown in the port velocity vectors in Figure 8(b). This flow impinges close to the corners between wide faces and NFs. As it flows

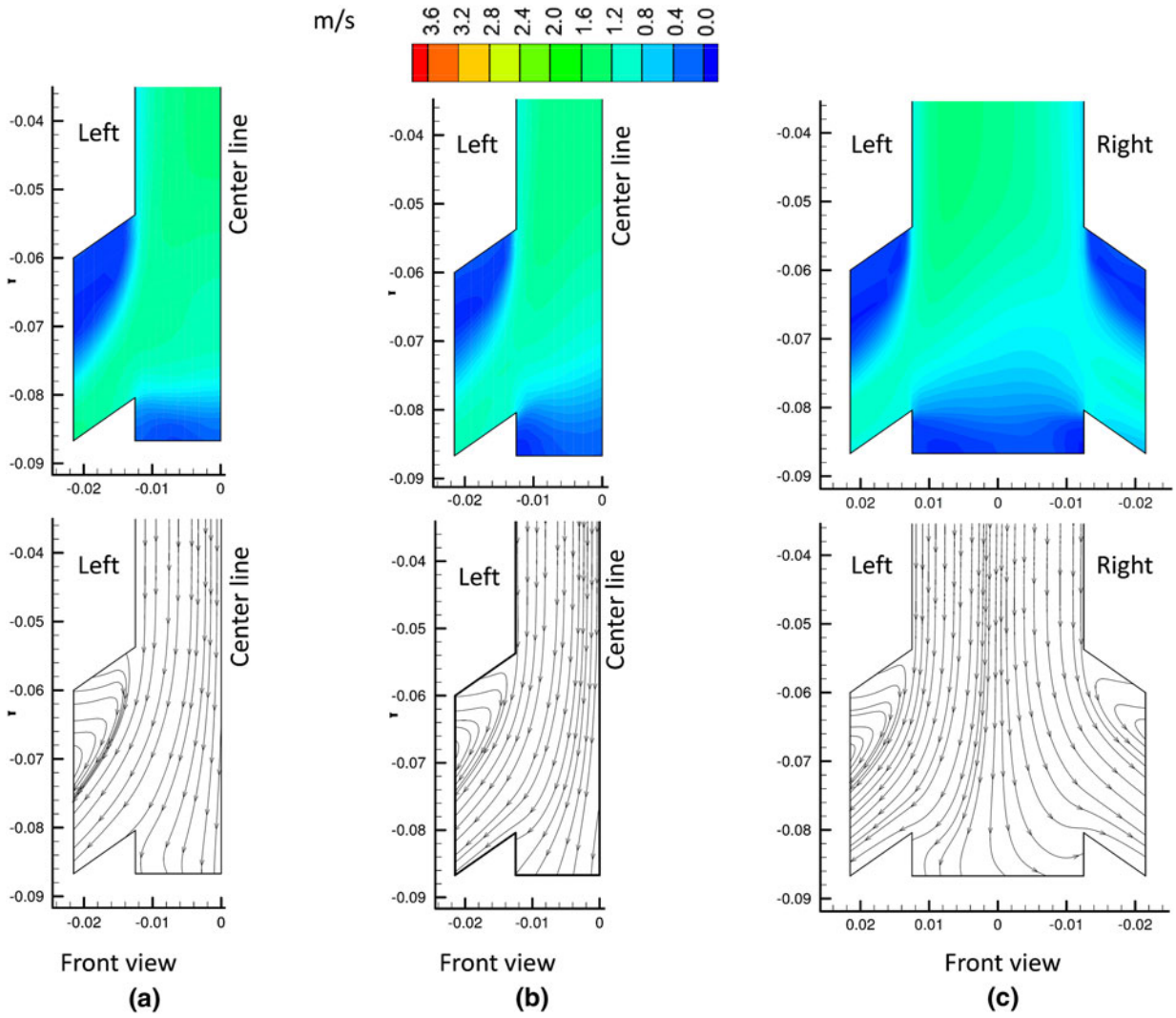

Fig. 7—Velocity contours and streamlines in the bottom portion of the nozzle with (*a*) aligned, (*b*) 2-mm front-misaligned, and (*c*) 2-mm left-misaligned stopper-rod.

up the NFs, the flow deflects toward the front side, leading to lower velocities in the midplane, as is shown in Figures 9(b) and 10. A smaller horizontal spread angle and a lower vertical jet angle give this case higher surface velocity than other cases, especially towards the front side.

In the left-misaligned stopper-rod case, the right port has a higher mass flow rate but a lower velocity compared with the left side (biased flow). The flow pattern created by this imbalance is shown at the mold midplane in Figure 9(c).

Vertical velocity down a path 10 mm from the NFs on each side of the SEN is shown in Figure 11 for all three cases. The jet hits almost at the same location (180 mm) on the left side of the three cases. On the right side of the left misalignment case, the jet impinges slightly higher (140 mm) than the other two cases. Left misalignment shows a stronger flow down the left side and weak reverse flow on the right side, owing to the asymmetric flow pattern.

B. *Surface Velocity*

Because of its importance on final product quality, the surface velocities predicted for the three cases are compared on both sides of the SEN in Figure 12. In the aligned stopper-rod case, even though the port velocity is highest, the steeper downward vertical jet angle and higher horizontal spread angle leads to less upward flow and weaker surface velocity. The surface velocity is highest with front misalignment and is lowest on the left side with left misalignment. With left misalignment, the shallower jet with a lower velocity but a higher flow rate on the right side gives a higher surface velocity on the right side.

The measured histories of horizontal surface velocity on both sides of the SEN are presented in Figure 13 for all 3 cases. The velocities measured by the impeller 15 mm below the surface are given at 60 mm (left) and 150 mm (right) from the NFs. The mean velocity on the left and right sides agree at both locations (*i.e.*, 60 mm

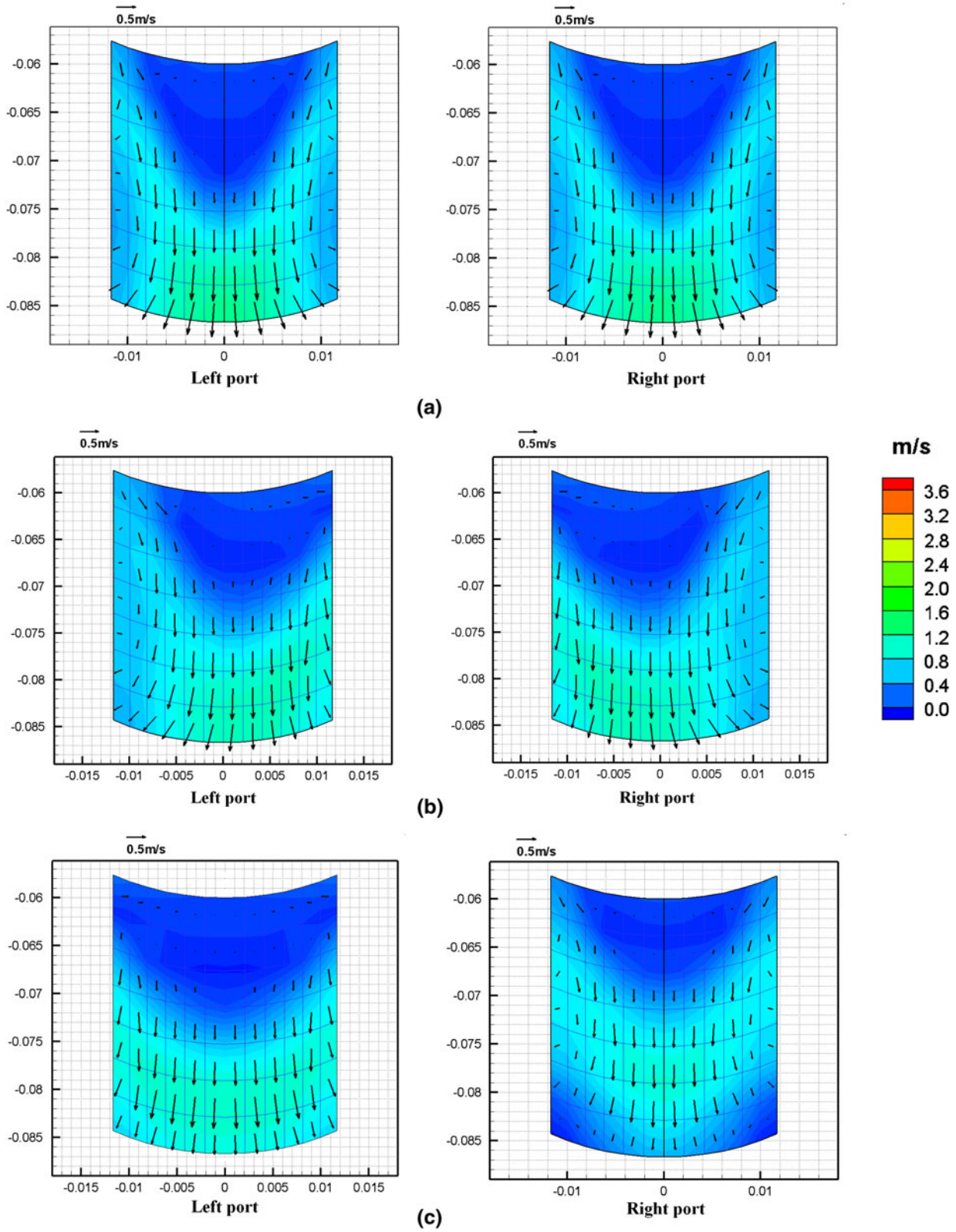

Fig. 8—Port velocities with (*a*) aligned, (*b*) 2-mm front misaligned, and (*c*) 2-mm left misaligned stopper-rod cases.

and 150 mm) within one standard deviation (Table II). Thus, the flow has right–left symmetry as expected with an aligned stopper. Asymmetry is worse at the 150-mm location (5 pct difference) than the 60-mm location (1 pct difference) because of the transient nature of the jet.

Table IV. Jet Characteristics of Aligned, Front-Misaligned, and Left-Misaligned Stopper-Rod Nozzle Ports' Jets

	Centered		Front-Misaligned Stopper-Rod		Left-Misaligned Stopper-Rod	
	Left	Right	Left	Right	Left	Right
Weighted average nozzle port velocity in x-direction (outward) (m/s)	0.66	0.66	0.68	0.68	0.73	0.69
Weighted average nozzle port velocity in y-direction (downward) (m/s)	0.53	0.53	0.51	0.51	0.53	0.35
Weighted average nozzle port velocity in z-direction (horizontal) (m/s)	0.058 (toward outward in half port)	0.058 (toward outward in half port)	0.022 (toward outer radius in full port)	0.022 (toward outer radius in full port)	0.055 (toward outward in half port)	0.021 (toward outward in half port)
Weighted average nozzle port turbulent kinetic energy (m^2/s^2)	0.060	0.060	0.026	0.026	0.020	0.028
Weighted average nozzle port turbulent kinetic energy dissipation rate (m^2/s^3)	3.24	3.24	1.15	1.15	0.83	1.29
Vertical jet angle (deg)	39.17	39.17	36.88	36.88	36.24	27.25
Horizontal jet angle (deg)	0	0	1.9	1.9	0	0
Horizontal spread (half) angle (deg)	5.08	5.08	—	—	4.33	1.76
Average jet speed (m/s)	0.85	0.85	0.85	0.85	0.91	0.78
Back-flow zone (pct)	19	19	19	19	28	12
Flow rate (pct)	50	50	50	50	45.62	54.38
Maximum velocity magnitude (m/s)	1.23	1.23	1.16	1.16	1.09	1.06

The front-misaligned case also exhibits the expected right–left symmetry (within one standard deviation). Again, asymmetry is worst at 150 mm (9 pct different) than at 60 mm (2 pct different). In the left-misaligned case, velocity is almost symmetric at 60 mm, (9 pct different). Asymmetry is clearly visible at 150 mm in this case, as the right side is 32 pct faster than the left because of the shallower jet on the right. This experimental finding of prominent asymmetry at 150 mm with a left-misaligned stopper-rod and higher velocity on the right side is consistent with the simulation results (Figure 12).

C. *Surface Level Profile*

A comparison of the free-surface level at the midplane on both sides of the SEN in all cases is given in Figure 14. The double-roll flow causes a higher surface near the NFs and SEN in all cases. Higher surface velocities cause higher level profile variations. The front-misaligned case shows the highest level near the NFs. The left side of the left-misalignment cases has the flattest surface, owing to the slower upward velocity along the left NF and the lower surface pressure from vortex formation on the left side of the SEN.

D. *Vortex Formation*

Transient mold flow, caused by wobbling jets, may cause intermittent chaotic vortex formation on both sides of the SEN in the mold cavity. In addition, right–left biased flows form more vortices on the left side, as explained earlier because of flow through the gap from the right. Figure 15(a) shows an example of vortex formation with the left-misaligned stopper-rod using sesame seeds to visualize surface entrainment. The vortex, forming preferentially on the left side as shown, carries sesame seeds down to the jet. In real casters, liquid mold slag entrapped in this way causes sliver defects which lower product quality.

Figure 15(b) presents the measured frequency of the vortex formation on both sides of the SEN for all three cases. All vortices are found in four regions close to the SEN. As expected, the formation frequency on the right and left sides is about the same (within 10 pct) in the aligned and front-misaligned cases. The front-misaligned case forms 26 pct more vortices than the aligned. The most vortices form on the left side of the left-misaligned case (*i.e.*, more than double the frequency produced on the right side). The right side of this case also has the least vortices (~30 pct less than the aligned case). These findings about vortices are consistent with the model-predicted and measured surface velocities.

Although the steady RANS k–ε turbulence model cannot predict vortex formation frequency, it can predict the location of the mean vortex through surface velocity vectors. Figure 15(c) shows the modeled surface velocity vectors in the left-misaligned stopper-rod case, clearly showing two vortices on the left side near the SEN, which reinforces the experimental findings. The standard k–ε model with standard wall laws performs best on a hexahedral coarse mesh, with symmetrical,

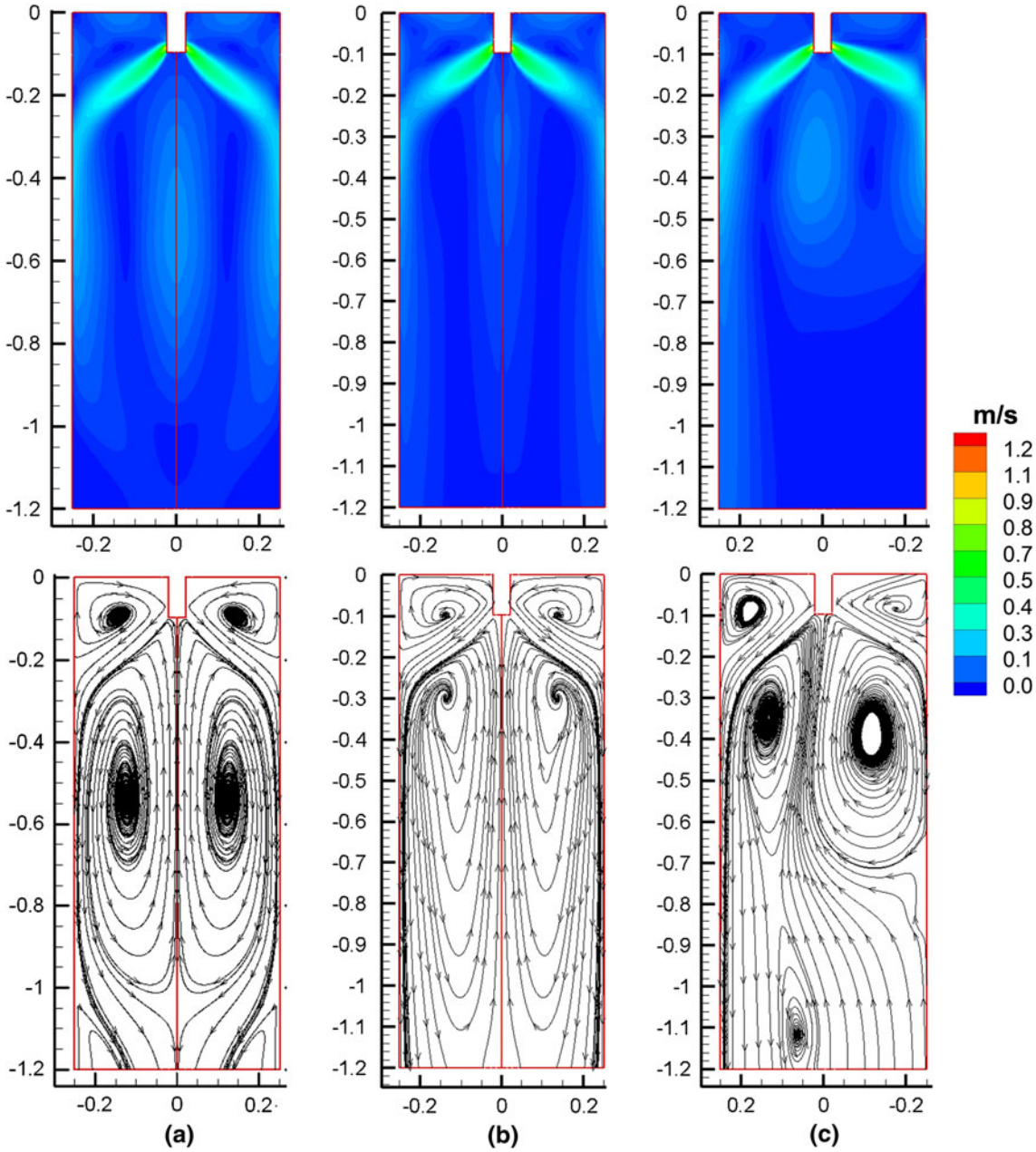

Fig. 9—Velocity contours and streamlines on the center plane between wide faces with (*a*) aligned, (*b*) 2-mm front-misaligned, and (*c*) 2-mm left-misaligned stopper-rod cases.

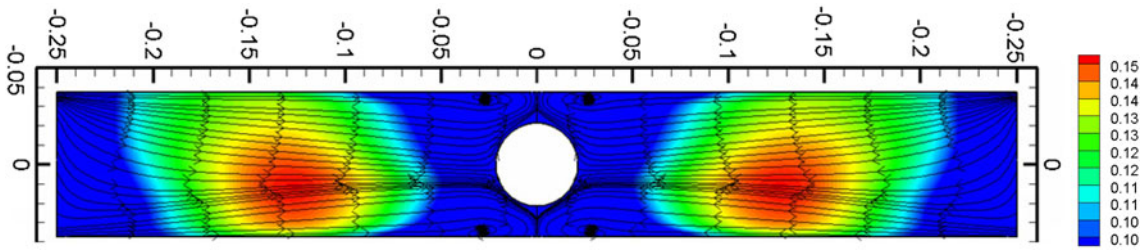

Fig. 10—Surface velocity contours with streamlines in front-misaligned stopper-rod case.

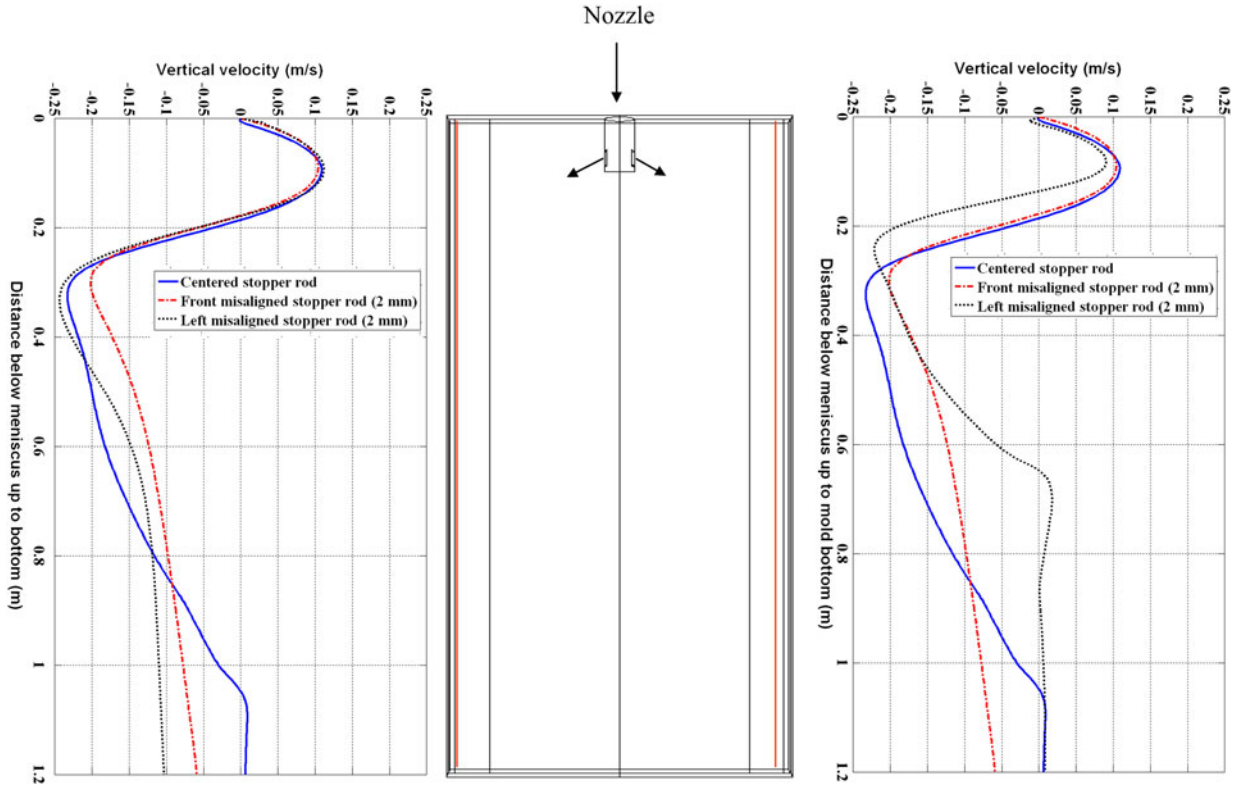

Fig. 11—Comparison of vertical velocities (at 10 mm from NFs along the mold length) on both sides of SEN comparing aligned, front-misaligned, and left-misaligned stopper-rod cases.

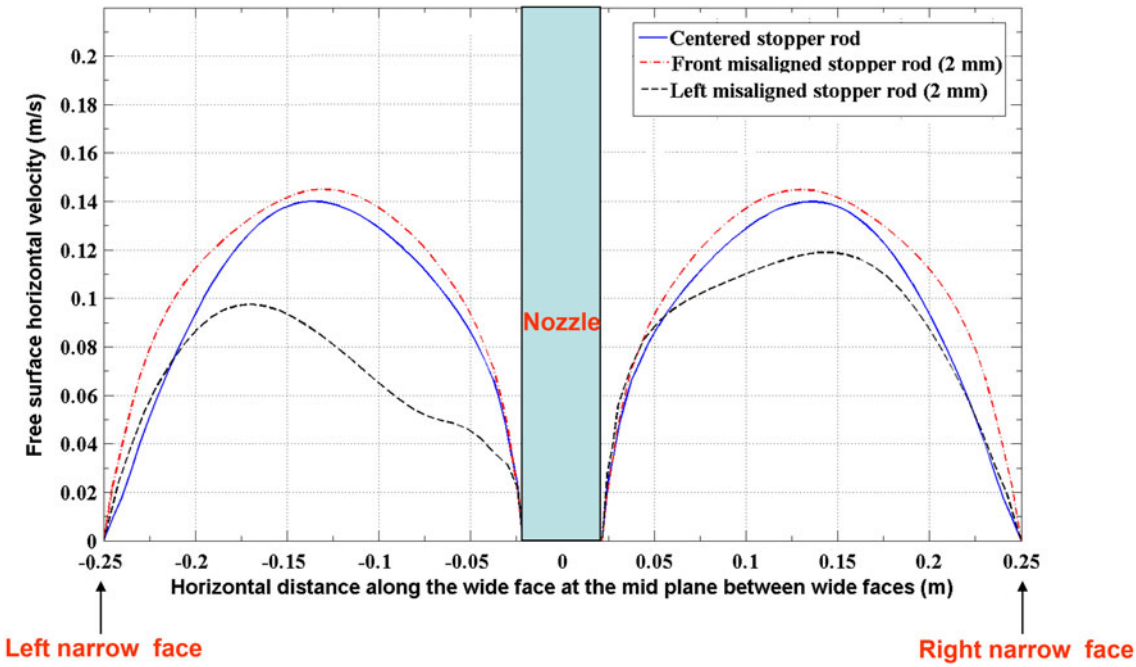

Fig. 12—Comparison of horizontal surface velocity magnitudes in aligned, front-misaligned, and left-misaligned stopper-rod cases.

well-shaped elements of similar size. Such a mesh was not possible for the complex asymmetric geometry of the misaligned nozzle, which explains why the predicted vortex shape is too elongated. More accurate predictions would require a transient computational model.

VI. CONCLUSIONS

In this article, the effect of stopper-rod misalignment on the fluid flow through a water model of continuous casting of steel has been investigated both

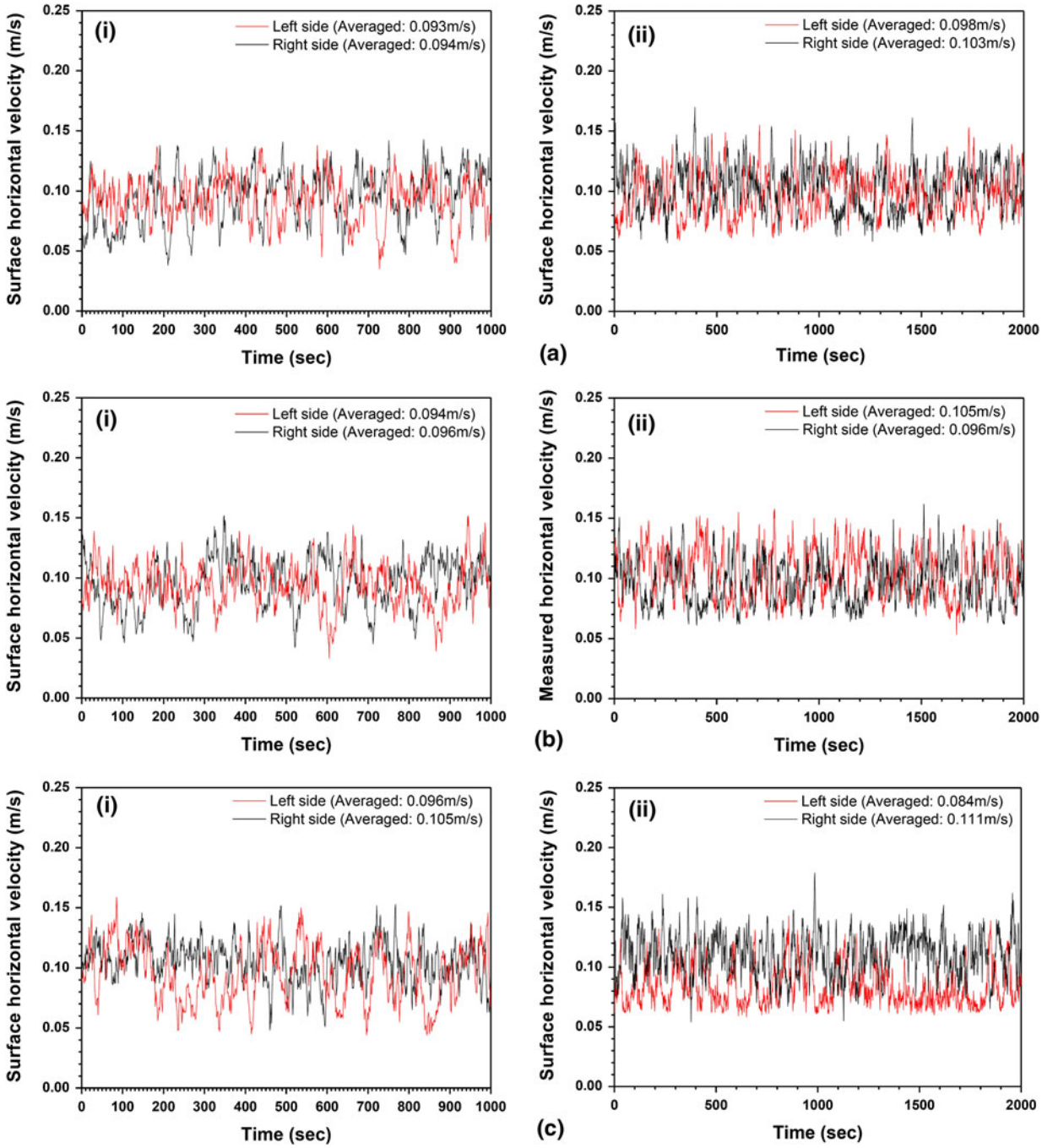

Fig. 13—Measured surface velocities with (*a*) aligned, (*b*) 2-mm front misaligned, and (*c*) 2-mm left misaligned stopper-rod ((i) Left figures: 60 mm from NFs, (ii) Right figures: 150 mm from NFs).

experimentally and numerically. The computational model matches well with the measured surface velocities and turbulent kinetic energies. The model predictions and measurements are consistent and together reveal new insights into the effects of stopper-rod misalignment.

With an aligned stopper-rod, flow and vortex formation show both right–left and back–front symmetry within the standard deviation of the measurements of ~20 pct. In front misalignment, flow from the UTN region with a higher momentum hits the bottom of the nozzle toward the front side and exits the front of the ports but is directed toward the back side of the mold (wide face). This causes front–back asymmetry in surface velocity. The surface velocity is right–left symmetric within the standard deviation of the measurements. With left misalignment, the higher momentum flow hits the left side of the SEN bottom, causing a thin, steep, high-velocity jet exiting the left port. The right port has a slower, shallower jet but with a higher mass flow rate

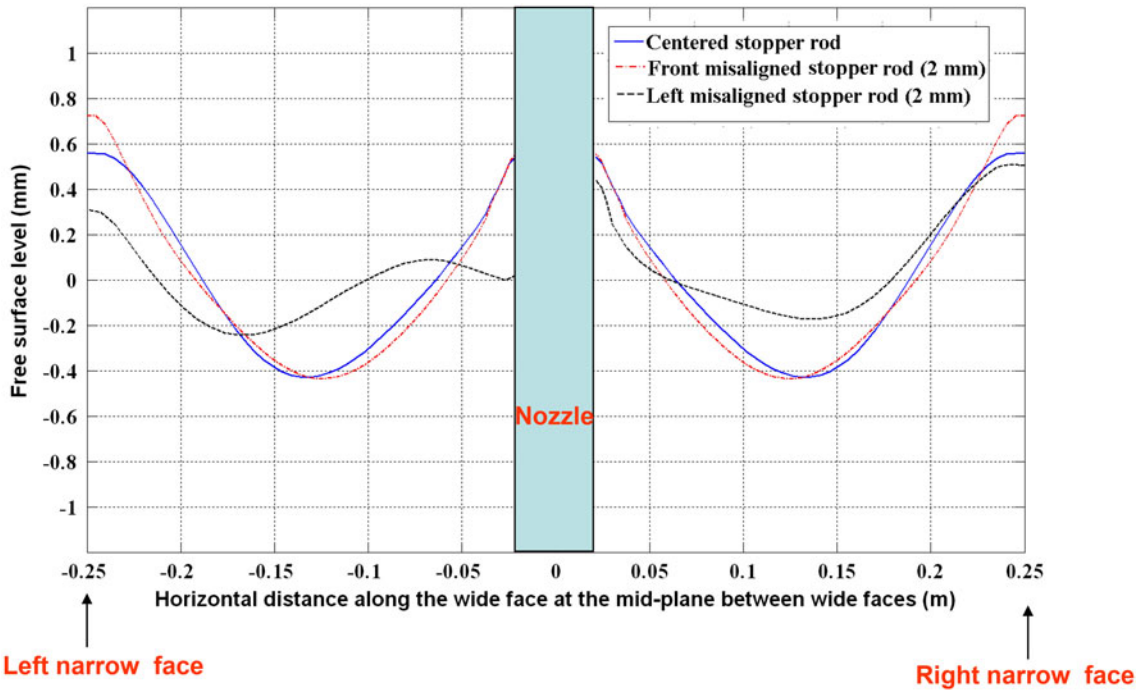

Fig. 14—Comparison of free surface levels in between aligned, front-misaligned, and left-misaligned stopper-rod cases.

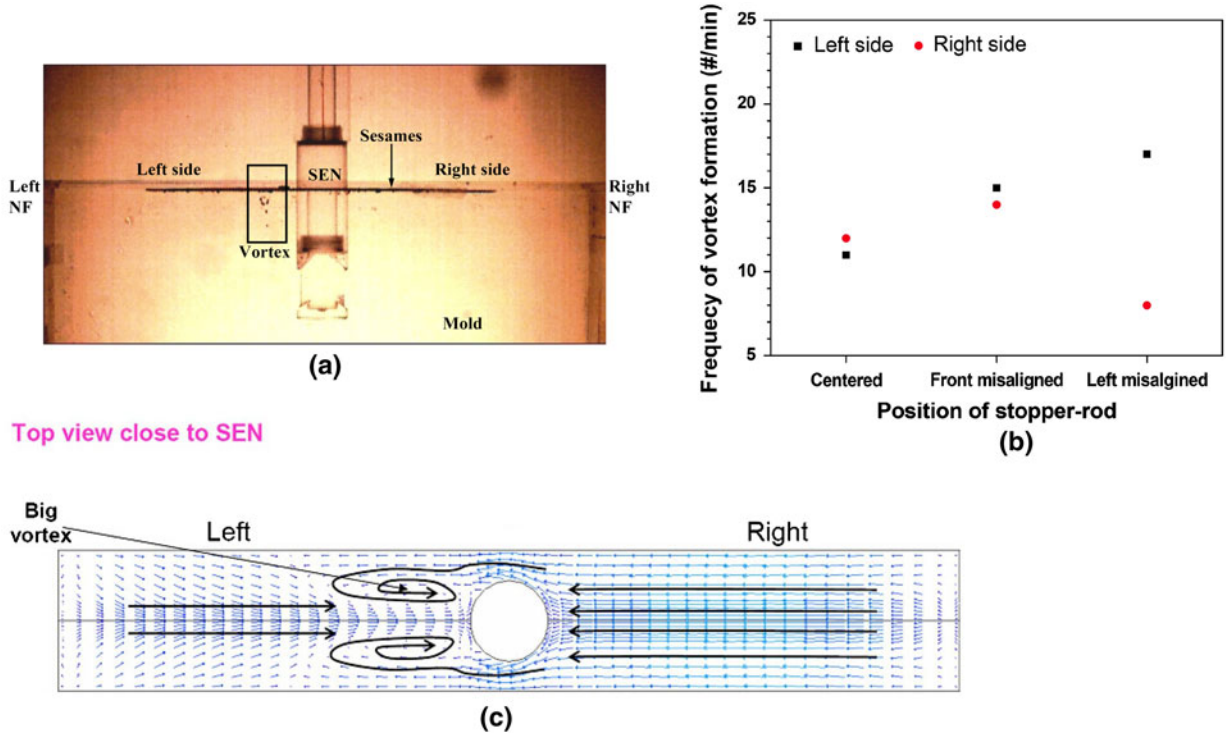

Fig. 15—(*a*) Experimental observation of vortex formation, (*b*) frequency of vortex formation around SEN in mold (60 mm), and (*c*) its RANS simulation with left misalignment.

(54 pct), which produces a higher surface velocity on the right side of this case. This right–left asymmetry on the surface velocity in this case is stronger close to the SEN (at 150 mm) where vortices form. These findings are consistent in both the simulations and the measurements.

Intermittent vortices form in all cases with similar frequencies on the right and left in the aligned and front-misaligned cases. The main cause of these vortices is the transient wobbling of the jet causing stronger surface flow from right to left at some times and from left to

right at other times. The right–left asymmetry in the measured surface velocities is higher close to the SEN in all cases. With left misalignment, the significant right–left asymmetry in velocity causes significantly more vortices to form on the left relative to the right. In summary, this study shows the importance of the alignment of stopper-rod in continuous casting and how a misaligned stopper causes significant asymmetric flow and increased formation of detrimental vortices.

ACKNOWLEDGMENTS

The authors thank POSCO and Shin-Eon Kang, POSCO Technical Research Laboratories for providing the water model, H.N. Bae for helping with the water model experiments, and ANSYS Inc. for supplying FLUENT. Support from the Continuous Casting Consortium, University of Illinois at Urbana-Champaign, POSCO, South Korea (Grant No. 4.0002397.01), and the National Science Foundation (Grant No. DMI 05-00453) is gratefully acknowledged.

REFERENCES

1. *World Steel in Figures*, International Iron and Steel Institute, Brussels, Belgium, 2007. www.worldsteel.org.
2. B.G. Thomas: in *Making, Shaping and Treating of Steel*, A.W. Cramb, ed., AISE Steel Foundation, Pittsburgh, PA, 2003.
3. J. Kubota, K. Okimoto, A. Shirayama, and H. Murakami: *Steelmaking Conf. Proceedings*, 1991.
4. S. Feldbauer and A. Cramb: *PTD Conf. Proc., 13*, Iron and Steel Society, Warrendale, PA, 1995, pp. 327–40.
5. J. Herbertson, Q.L. He, P.J. Flint, and R.B. Mahapatra: *Steelmaking Conf. Proc. 1991*, Iron and Steel Society, Warrendale, PA, pp. 171–85.
6. T. Honeyands and J. Herbertson: *Steel Res. Int.*, 1995, vol. 66, pp. 287–93.
7. W.H. Emling, T.A. Waugaman, and S.L. Feldbauer: *77th Steelmaking Conference Proc*, Iron and Steel Society, Warrendale, PA, 1994.
8. Q. Yuan, B.G. Thomas, and S.P. Vanka: *Metall. Mater. Trans. B.*, 2004, vol. 35B, pp. 685–702.
9. H. Bai and B.G. Thomas: *Metall. Mater. Trans. B*, 2001, vol. 32B, pp. 253–67.
10. H. Bai and B.G. Thomas: *Metall. Mater. Trans. B*, 2001, vol. 32B, pp. 269–84.
11. G.-G. Li, H.-J. Shin, B.G. Thomas, and S.-H. Kim: *AISTech Iron and Steel Technology Conf. 2008*, Pittsburgh, PA, 2008.
12. S. Mahmood: MS Thesis, University of Illinois at Urbana-Champaign, 2006.
13. L. Zhang, Y. Wang, and X. Zuo: *Metall. Mater. Trans. B*, 2008, vol. 39B, pp. 534–50.
14. S. Yokoya, S. Takagi, M. Iguchi, K. Marukawa, and S. Hara: *ISIJ Int.*, 2001, vol. 41, pp. 1215–20.
15. D. Gupta, S. Chakraborty, and A.K. Lahiri: *ISIJ Int.*, 1997, vol. 37, pp. 654–58.
16. D. Gupta and A.K. Lahiri: *Metall. Mater. Trans. B*, 1996, vol. 27B, pp. 757–64.
17. B.K. Li, T. Okane, and T. Umeda: *Metall. Mater. Trans. B*, 2001, vol. 32B, pp. 1053–66.
18. B. Li and F. Tsukihashi: *ISIJ Int.*, 2005, vol. 45, pp. 30–36.
19. Q. Yuan, B. Zhao, S.P. Vanka, and B.G. Thomas: *Steel Res. Int.*, 2005, vol. 76, pp. 33–43.
20. H.K. Versteeg and W. Malalasekra: *An Introduction to Computational Fluid Dynamics: The Finite Volume Method Approach*, Longman Scientific Technical, Essex, England, 1995.
21. S.-M. Cho, G.-G. Lee, S.-H. Kim, R. Chaudhary, O.-D. Kwon, and B.G. Thomas: *2010 TMS Annual Meeting & Exhibition*, Seattle, WA, 2010.
22. B.E. Launder and D.B. Spalding: *Mathematical Models of Turbulence*, Academic Press, London, U.K, 1972.
23. ANSYS Inc., *FLUENT6.3-Manual*, 2007, ANSYS Inc., Lebanon, NH.
24. D.E. Hershey, B.G. Thomas, and F.M. Najjar: *Int. J. Num. Meth. Fluids*, 1993, vol. 17, pp. 23–47.
25. X. Huang and B.G. Thomas: *Can. Metall. Q.*, 1998, vol. 37, pp. 197–212.
26. G.A. Panaras, A. Theodorakakos, and G. Bergeles: *Metall. Mater. Trans. B*, 1998, vol. 29B, pp. 1117–26.
27. B.E. Launder and D.B. Spalding: *Comput. Meth. Appl. Mech. Eng.*, 1974, vol. 3, pp. 269–89.
28. R. Chaudhary, G.-G. Lee, B.G. Thomas, and S.-H. Kim: *Metall. Mater. Trans. B*, 2008, vol. 39B, pp. 870–84.
29. R. Chaudhary, B.G. Thomas, and S.P. Vanka: "Department of Mechanical Science and Engineering", CCC Report 201011, University of Illinois at Urbana-Champaign, IL, 2010.
30. H. Bai and B.G. Thomas: *Metall. Mater. Trans. B*, 2001, vol. 32B, pp. 253–67.
31. F.M. White: *Fluid Mechanics*, 4th ed., Mc-Graw Hill, New York, NY, 1999.
32. R. Chaudhary, B.T. Rietow, and B.G. Thomas: *Materials Science and Technology Conf*, AIST/TMS, Pittsburgh, PA, 2009.